

Article

Sentinel-1A/B Combined Product Geolocation Accuracy

Adrian Schubert ^{1,*}, Nuno Miranda ², Dirk Geudtner ³ and David Small ¹

¹ Remote Sensing Laboratories, University of Zurich, Winterthurerstrasse 190, 8057 Zurich, Switzerland; david.small@geo.uzh.ch

² ESA-ESRIN, Via Galileo Galilei, 00044 Frascati, Italy; nuno.miranda@esa.int

³ ESA-ESTEC, Keplerlaan 1, 2200 AG Noordwijk, The Netherlands; dirk.geudtner@esa.int

* Correspondence: adrian.schubert@geo.uzh.ch; Tel.: +41-44-635-6523

Academic Editors: Bruce Chapman, Paul Siqueira and Prasad S. Thenkabail

Received: 28 April 2017; Accepted: 9 June 2017; Published: 14 June 2017

Abstract: Sentinel-1A and -1B are twin spaceborne synthetic aperture radar (SAR) sensors developed and operated by the European Space Agency under the auspices of the Copernicus Earth observation programme. Launched in April 2014 and April 2016, Sentinel-1A and -1B are currently operating in tandem, in a common orbital configuration to provide an increased revisit frequency. In-orbit commissioning was completed for each unit within months of their respective launches, and level-1 SAR products generated by the operational SAR processor have been geometrically calibrated. In order to compare and monitor the geometric characteristics of the level-1 products from both units, as well as to investigate potential improvements, products from both satellites have been monitored since their respective commissioning phases. In this study, we present geolocation accuracy estimates for both Sentinel-1 units based on the time series of level-1 products collected thus far. While both units were demonstrated to be performing consistently, and providing SAR data products according to the nominal product specifications, a subtle beam- and mode-dependent azimuth bias common to the data from both units was identified. A method for removing the bias is proposed, and the corresponding improvement to the geometric accuracies is demonstrated and quantified.

Keywords: Synthetic Aperture Radar (SAR); Sentinel-1; geolocation calibration/validation

1. Introduction

The Sentinel-1 (S-1) Mission, as part of the space component of Copernicus, is based on a constellation of two satellites that fulfil revisit and coverage requirements, providing robust datasets for Copernicus services. The S-1 Mission has been specifically designed by the European Space Agency (ESA) to systematically acquire data and information products for Copernicus ocean, land and emergency services, as well as to national user services [1,2].

Sentinel-1A was successfully launched on 3 April 2014; it was followed by the launch of Sentinel-1B on 25 April 2016. Both satellite units, Sentinel-1A (S-1A) and Sentinel-1B (S-1B), fly in a quasi-polar, sun-synchronised (dawn–dusk) orbit at 693 km altitude, and in the same orbital plane 180° out of phase with each other [1,2].

Data products from synthetic aperture radar (SAR) sensors that have been accurately geometrically calibrated permit a straightforward combination of multiple data takes with one another [3], not only simplifying their inter-comparison, but also speeding up applications such as near-real-time disaster mapping. High quality geolocation is required for SAR interferometric processing, such as during image co-registration using the annotated timing information and orbital data [4]. In comparison to S-1's predecessor ENVISAT ASAR [5,6], the geolocation accuracy of S-1 has been shown to be much

improved [7–9]. The improved orbit state vector quality is reflected in the small residual baseline fringes in interferograms [10].

Given the rapidly growing dense time series from S-1 and other sensors, accurate product co-registration is quickly gaining in importance. The extremely high accuracy of modern SAR sensors such as TerraSAR-X (TSX) [11–13] and S-1 [7–9] is opening doors to new applications, such as using products as geodetic references for less well calibrated optical images [14], or the joint creation of SAR-GNSS (SAR-Global Navigation Satellite Systems) geodetic networks for deformation monitoring [15].

Beyond applications such as interferometric SAR (InSAR), an improved geolocation accuracy enables the establishment of a “blind” connection between the radar images and, e.g., a Digital Elevation Model (DEM), which is essential for applications such as radiometric terrain flattening [16]. No correlation with a simulated image is necessary to “refine” the initially annotated imaging geometry [17]: radiometric terrain flattening may proceed without that unnecessary intermediate step.

The geometric calibration of a SAR system involves the determination of systematic timing offsets in the SAR system, such as between the radar and Global Positioning System (GPS) time (i.e., azimuth or along-track) and the internal electronic delay of the SAR instrument itself (i.e., the range delay time). These types of timing offsets cause systematic offsets in the SAR images’ pixel locations. The determination of the timing offsets is usually accomplished using trihedral corner reflectors (CR), as has been performed in the past for ENVISAT ASAR [5,6] and the German Aerospace Centre’s (DLR) TSX/TanDEM-X constellation [3,11–13,15].

1.1. Swiss Test Sites

The geometric calibration results of the S-1A’s in-orbit commissioning phase were presented in [9]. The study was performed on the basis of two test sites in Switzerland: *Torny-le-Grand* and *Dübendorf*. For S-1B’s commissioning, these sites were re-used, but with some changes to the corner reflector arrangement. Prior to the S-1B launch in 2016, two 1.5 m trihedral corner reflectors were acquired, similar to those available for S-1A’s commissioning, but slightly larger (shown in Figure 1a). Both were deployed in *Torny-le-Grand* on paved concrete surfaces within a secure area. One was oriented towards a “mean” S-1 ascending orbit, and the other towards a descending orbit.

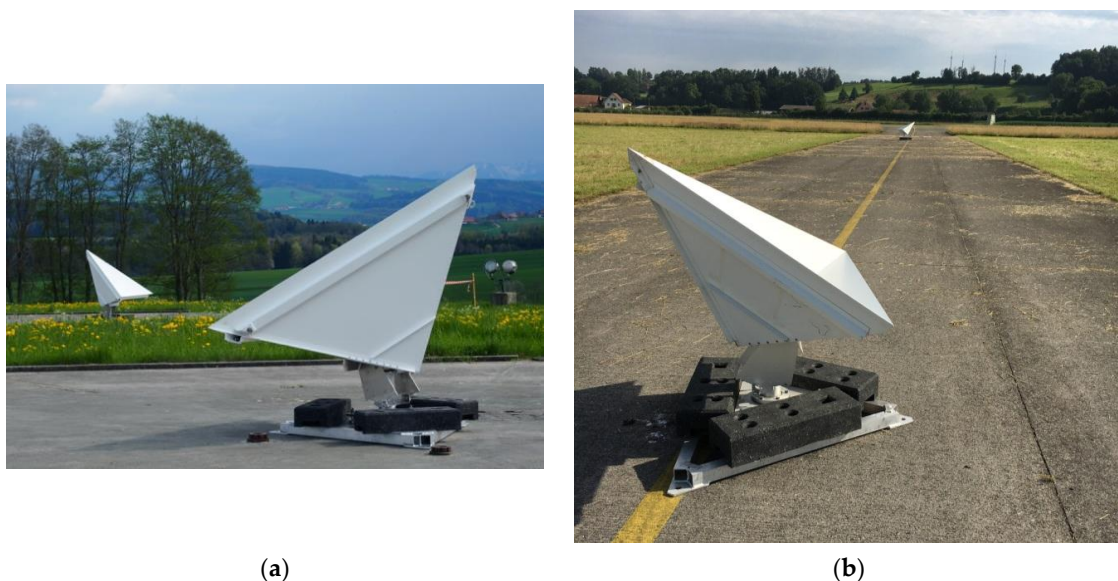


Figure 1. Trihedral corner reflectors at test sites in Switzerland, used for Sentinel-1B’s (S-1B) calibration as well as Sentinel-1A/B product validation; (a) 1.5 m reflectors near *Torny-le-Grand*; (b) 1.0 m (foreground) and 1.2 m reflectors (background) near *Dübendorf*.

In *Diibendorf*, a similar arrangement was organised, using 1.2 m and 1.0 m reflectors (Figure 1b). The first geolocation tests during S-1B commissioning were promising [18], with the lessons and methods implemented since S-1A's commissioning having been already applied.

1.2. Australian Test Site

Since November 2014, Geoscience Australia (GSA) has been operating a unique corner reflector test site ~200 km west of Brisbane, Australia, within the Surat Basin (as described in [19]). Initially intended for long-term monitoring using SAR interferometry, it includes 40 trihedral corner reflectors facing a typical S-1 ascending orbit, and distributed over an area of $\sim 120 \times 120$ km. Thirty-four reflectors have 1.5 m side lengths, and three each of 2.0 m and 2.5 m side length are included as well.

As part of an ongoing combined product/site validation campaign, a time series of Interferometric Wide Swath (IW) mode, slant range complex (SLC) products (99 in total) has been collected since March 2015. Ultimately, it is hoped that the SAR products acquired over this site will allow for geometric (and radiometric) measurements on par with the sites in Switzerland and elsewhere. For now, the site has been used as an additional route to seek out data problems in common with those acquired over Switzerland, while at the same time helping to understand the advantages and limitations of such a corner reflector array.

2. Products and Methods

2.1. SAR Products Tested

An overview of the S-1 data products tested is provided in Table 1. Both single look complex (SLC) and ground range detected (GRD) products from S-1's StripMap (SM), Interferometric Wide Swath (IW), and Extended Wide Swath (EW) modes were included in this study. The highest resolution GRDs were analysed for a given mode: GRDF (fine resolution) products for the SM mode and GRDH (high resolution) products for the IW/EW modes. In order to include as many observations as possible for a given product type, all of the acquisitions currently available were used, including data acquired during the S-1A and S-1B in-orbit commissioning phases. Only products that were considered reliable were included, as indicated by the quality of the imaged targets and quantified in the form of the signal to clutter ratio (SCR). This parameter describes the degree of clarity and contrast of the imaged reflector. With decreasing SCR, the imaged target looks correspondingly less "sharp", and its shape (response function) more poorly defined. This may happen, e.g., if the reflector's drainage holes become clogged and the reflector fills partly with water (or snow during the winter).

Table 1. Number and types of Sentinel-1 (S-1) products used for absolute location error (ALE) estimation.

| Acq. Mode | Product Type | Number of Products | Date Range |
|-----------|--------------|--------------------|--------------------------------|
| SM | SLC | 65 | 7 June 2014–16 September 2016 |
| | GRDF | 60 | 31 July 2014–16 September 2016 |
| IW | SLC | 194 | 12 June 2014–27 March 2017 |
| | GRDH | 133 | 4 November 2014–27 March 2017 |
| EW | SLC | 43 | 25 June 2016–21 December 2016 |
| | GRDH | 38 | 25 June 2016–21 December 2016 |

The selection of the SCR threshold was empirical, defined for each product type, and based mainly on complementary knowledge of the reflector condition. For example, if it was known that a reflector was partially filled with rainwater or snow, the measured SCR was assumed to be below the desired threshold. By comparing the measured SCR and the known conditions at the test sites, threshold values were determined that reliably eliminated targets having high chances of being distorted in

the image products. While this did eliminate several potentially false positives, the conservative operational assumption was that the entire range of SCR values corresponding to partially water- or snow-filled reflectors should be considered unreliable, even if this range occasionally included images with no known perturbing influences.

For sensor characterisation and calibration purposes, the SM SLC products offered the best available instrument fidelity. They offer the highest spatial resolution (typically $\sim 2.5 \times 4$ m in slant range and azimuth), and the SLC products contain the recorded echo amplitude and phase information after focusing. All of the other S-1 products tested here are either not as well spatially resolved, or have been detected and multi-looked. For these reasons, the SM SLC products are especially important during the determination of the range bias subsequently used by the operational SAR processor.

However, as IW is the main mode of operation over the land masses, special attention was paid to the IW SLC products in this study. Their spatial resolution is typically in the order of $\sim 3 \times 20$ m in slant range and azimuth.

Enough EW mode products were collected to allow for a reliable estimate of their geolocation accuracies as well. The resolution of the EW SLC products (typically $\sim 10 \times 40$ m in slant range and azimuth) is significantly lower than their IW cousins, but, especially over the 1.5 m reflectors in *Torny-le-Grand*, the target images were bright enough to permit relatively reliable geolocation testing.

For all three acquisition modes, geolocation tests were performed on the highest-resolution GRD products available for that mode (high-resolution GRDH for IW and EW, and fine-resolution GRDF for SM). This was done primarily in order to validate the products, and look for unexpected deviations.

2.2. Product Geolocation Accuracy Specifications

The required S-1 product absolute location accuracies at 3σ are given nominally in [20] by mode: SM products are expected to have 2.5 m accuracy; IW is specified at 7 m; and EW is “not specified”. In other words, the region defined by three standard deviations from the mean (in each dimension) should lie fully within the specified boundaries.

2.3. Absolute Location Error Estimation

At the core of the test for geolocation accuracy is a comparison between the surveyed location of a reflector vertex and its measured location in a SAR image. Given the radar timing annotations (time of first range sample, range sampling rate, first azimuth time, azimuth sample interval) and the state vectors describing the satellite’s trajectory during the time of data acquisition, a point on the Earth’s surface may be located within the image by solving the range-Doppler equations governing the image product’s geometry. The prediction is then adjusted for known perturbing effects such as the atmospheric path delay (APD), solid Earth tide (SET), and tectonic plate movement affecting the GPS position, which are described in detail in [13] and [9]. Also, the predicted azimuth (along-track) locations are corrected for the “bistatic residual”, which is a range-dependent azimuth timing correction described already for S-1A in [9]. The correction compensates for small deviations of the radar product timing annotations from the zero-Doppler imaging geometry.

The difference between the *predicted* target location in the image and its *measured* location (obtained with sub-sample accuracy) is the absolute location error (ALE), generally expressed in the slant range and azimuth dimensions separately.

The appearance of a 1.5 m reflector in the SM SLC and the IW SLC products is illustrated in Figure 2. The imagerettes are extracts from the SAR products; the crosshairs indicate the predicted target location based on the product annotations. In both cases, the SCR is high enough to begin to see the target sidelobes (forming the typical “cross pattern” following the expected *sinc* envelope of the impulse response function). The centre of each “cross” corresponds to the reflector’s vertex.

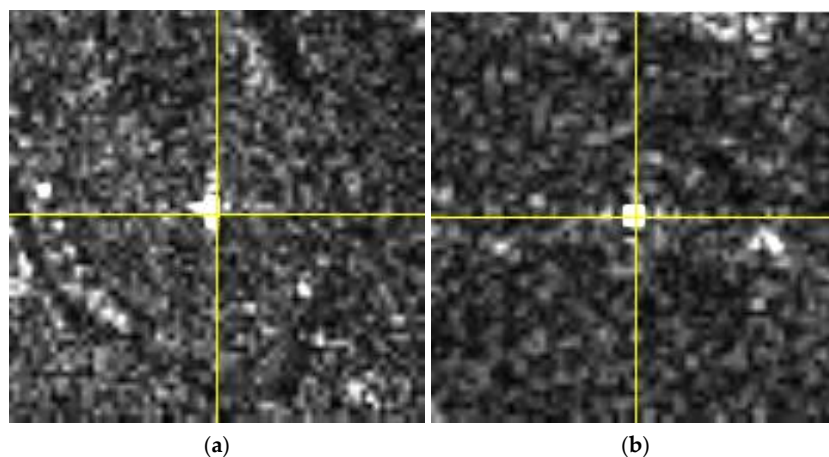


Figure 2. Appearance of the same 1.5 m corner reflector (such as shown in Figure 1a) in two S-1 product image extracts: (a) S1-B SM SLC; (b) Sentinel-1A (S-1A) IW SLC. The extracts are 70×70 samples large, and the target was viewed with a 37.0° local incident angle in the SM case, 45.7° in the IW case. Yellow crosshairs indicate predicted phase centres (peak intensities) based on the provided annotations and model-based corrections for perturbations (such as atmospheric path delay). The signal to clutter ratio was measured to be 36.8 dB in the SM case (a), and 29.3 dB for the IW product in (b). Copernicus Sentinel data (2016).

3. S-1A/B Geolocation Estimates over Swiss Test Sites

ALE scatterplots were generated for all of the S-1 product time series described in Section 2.1. Only the SLC product plots are shown, as these have the highest spatial resolution for a given mode (while also retaining the phase information). There were no unexpected trends or features visible in the GRD scatterplots. The lower product resolution in comparison to the respective SLC from a given mode causes the GRDs to have high standard deviations, but the mean offsets were similar to those of the SLCs. The GRD product ALE statistics are listed along with the SLC statistics in Table 2.

An important illustrative feature of the ALE scatterplots shown in the following sections is the symbol colour scheme. Colours indicate either an SM beam or an IW/EW subswath. In the plots shown below, they highlight the apparent relationship between beam/subswath and azimuth ALE, hypothesised to reflect a residual error in the processor, as discussed later.

Table 2. Product ALE estimates for S-1A/B acquisitions over Swiss test sites. The right-hand column shows azimuth ALE values after beam-dependent azimuth correction.

| Acq. Mode | Product Type | Number of Products | ALE (Mean \pm σ) (m) | | |
|-----------|--------------|--------------------|--------------------------------|-----------------------------------|-----------------------------------|
| | | | Slant Range | Azimuth (Uncorrected) | Azimuth (Corrected) |
| SM | SLC | 65 | -0.03 ± 0.07 | 1.82 ± 0.23 | 0.00 ± 0.12 |
| | GRDF | 60 | -0.02 ± 0.19 | 1.87 ± 0.37 | 0.00 ± 0.28 |
| IW | SLC | 194 | 0.15 ± 0.19 | 1.44 ± 1.19 | 0.00 ± 0.55 |
| | GRDH | 133 | 0.20 ± 0.24 | 0.31 ± 1.31 | - |
| EW | SLC | 43 | -0.35 ± 0.54 | 2.19 ± 4.07 | 0.00 ± 2.13 |
| | GRDH | 38 | -0.27 ± 1.18 | 0.41 ± 3.77 | - |

3.1. StripMap (SM) Mode

In Figure 3a–c, ALE scatterplots are shown for the beam S-1 SLC products collected over the Swiss test sites. The inverted triangles symbolise products from descending orbits; the triangles pointed upwards indicate ascending orbits. The highest quality precise orbit files (AUX_POEORB) were used during geolocation for all of the products. While there is currently no azimuth timing calibration support in the S-1 processor, future versions of the processor will include azimuth calibration constants. This will shift the mean azimuth ALE to \sim zero and move it even further into the 3σ requirement.

Figure 3a,b shows the S-1A and S-1B scatter separately; Figure 3c shows the combined scatter. The separate S-1A/B plots were made to check for potential relative biases, especially in azimuth as no azimuth calibration constants were applied by the S-1 Instrument Processing Facility (IPF) i.e., the S-1 processor. The symbol colouring indicates the SM beam. When comparing Figure 3a (S-1A) and Figure 3b (S-1B), it can be seen that S-1A and S-1B appear to be compatible; the combined ALE shown in Figure 3c may therefore be considered a valid reflection of S-1's constellation geolocation accuracy. Two products (from beams S2 and S6, shown in red and blue near the bottom and top of Figure 3c) appear to be outliers. However, no abnormally low SCR was seen in these products, and they were retained in the plot.

Figure 3d shows the same ALE scatter in a different way: the azimuth ALE is plotted as a function of slant range time (i.e., proportional to the target range). The slant range limits of the beams are shown via the coloured areas. A linear least-squares fit is shown on top of the scatter. There appears to be a linear correlation between the slant range and the azimuth offset (at least at the beam-by-beam level). This reminds us superficially of the "bistatic residual" correction mentioned in Section 2.3, which is described in detail for S-1A in [9]. The bistatic residual is an azimuth timing error (corresponding to an ALE error), which increases with increasing distance from a reference slant-range. If left uncorrected, it results in a range-dependent azimuth error not unlike the one visible in Figure 3d, but with a significantly steeper slope.

However, while Figure 3d appears to suggest an overall dependency of azimuth offset on slant range, the apparent range dependency disappears if one considers only the individual beams. Especially in beams S2 and S4, where several data points exist for more than one range position, there is no apparent range trend. This suggests a *beam-specific* offset rather than a *range-dependent* one. However, the small number of points available in a given beam does not permit a more conclusive interpretation based on these data alone. The beam dependency hypothesis was, on the other hand, supported using TOPS-mode (Terrain Observation by Progressive Scans, i.e., IW- and EW-mode) product scatter plots, as discussed in the following sections.

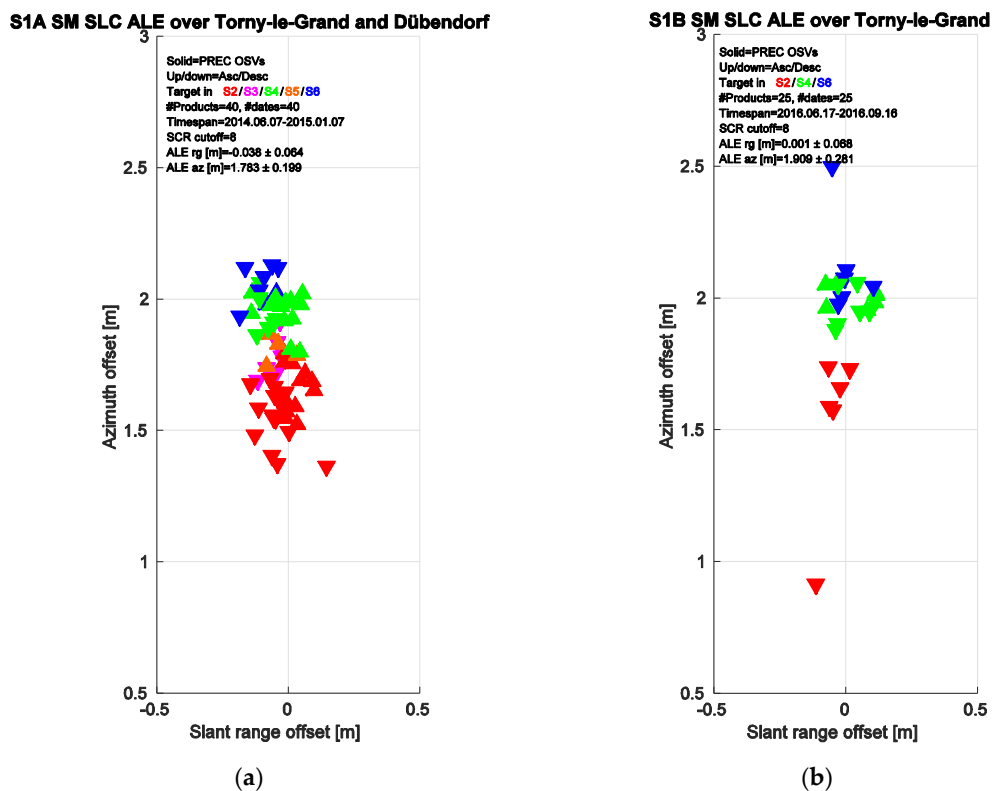


Figure 3. Cont.

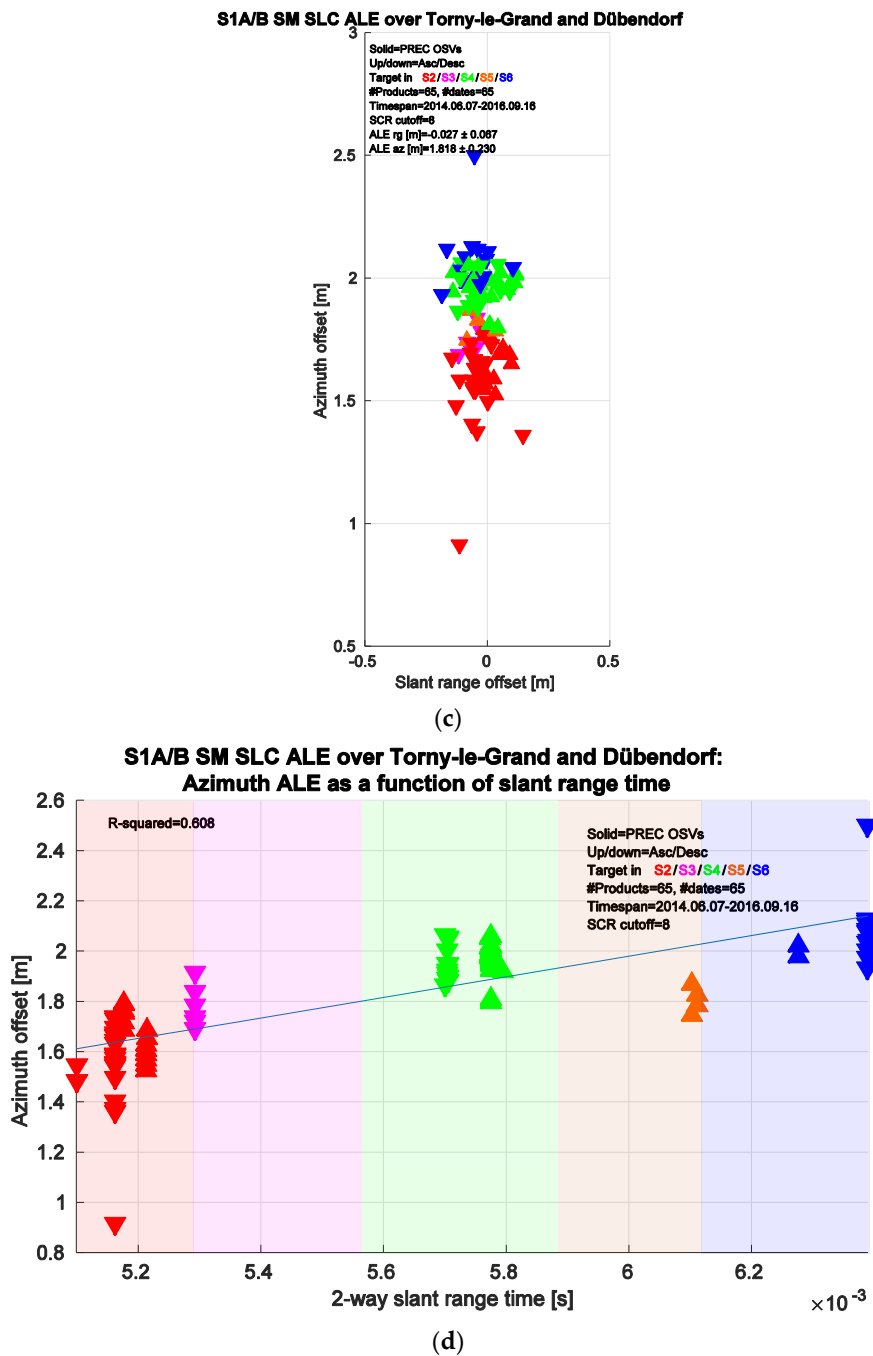


Figure 3. S-1A/B SM mode SLC product geolocation accuracy based on products over the Swiss test sites between 2014 and 2016: (a) S-1A; (b) S-1B; (c) S-1A/B combined; (d) azimuth error vs. slant range time for SM mode SLC products, with least-squares fit. Coloured regions indicate approximate beam ranges.

3.2. Interferometric Wide Swath (IW) Mode

An S-1A/B ALE scatter was generated for the IW SLC products acquired from 2014 to 2017 as shown in Figure 4. As with the SM mode, the S-1A and S-1B plots are shown both separately (Figure 4a,b) and merged (Figure 4c). As before, the S-1A/-B plots are consistent with each other, supporting the validity of a merged plot. The hollow marker visible in Figure 4b indicates the use of a near-real-time restituted (AUX_RESORB file) orbit during geolocation. As previously demonstrated, the restituted orbits are nearly as reliable as the precise orbits [9], rendering their effect here negligible, especially in light of the 7 m 3σ requirement mentioned in Section 2.2.

In Figure 4d, the dependency of the azimuth offset on the slant range is shown again, as it was for the SM mode in Figure 3d. Interestingly, the inverse of the SM dependency is observed for the IW mode: the azimuth offset *decreases* with increasing range (corresponding to an increasing subswath number), whereas for SM it was the reverse. What Figures 3d and 4d have in common is an apparent grouping by subswath (or beam), with no apparent range trend within a given subswath. This provides further evidence of a subswath- (and not a range-) dependent azimuth offset.

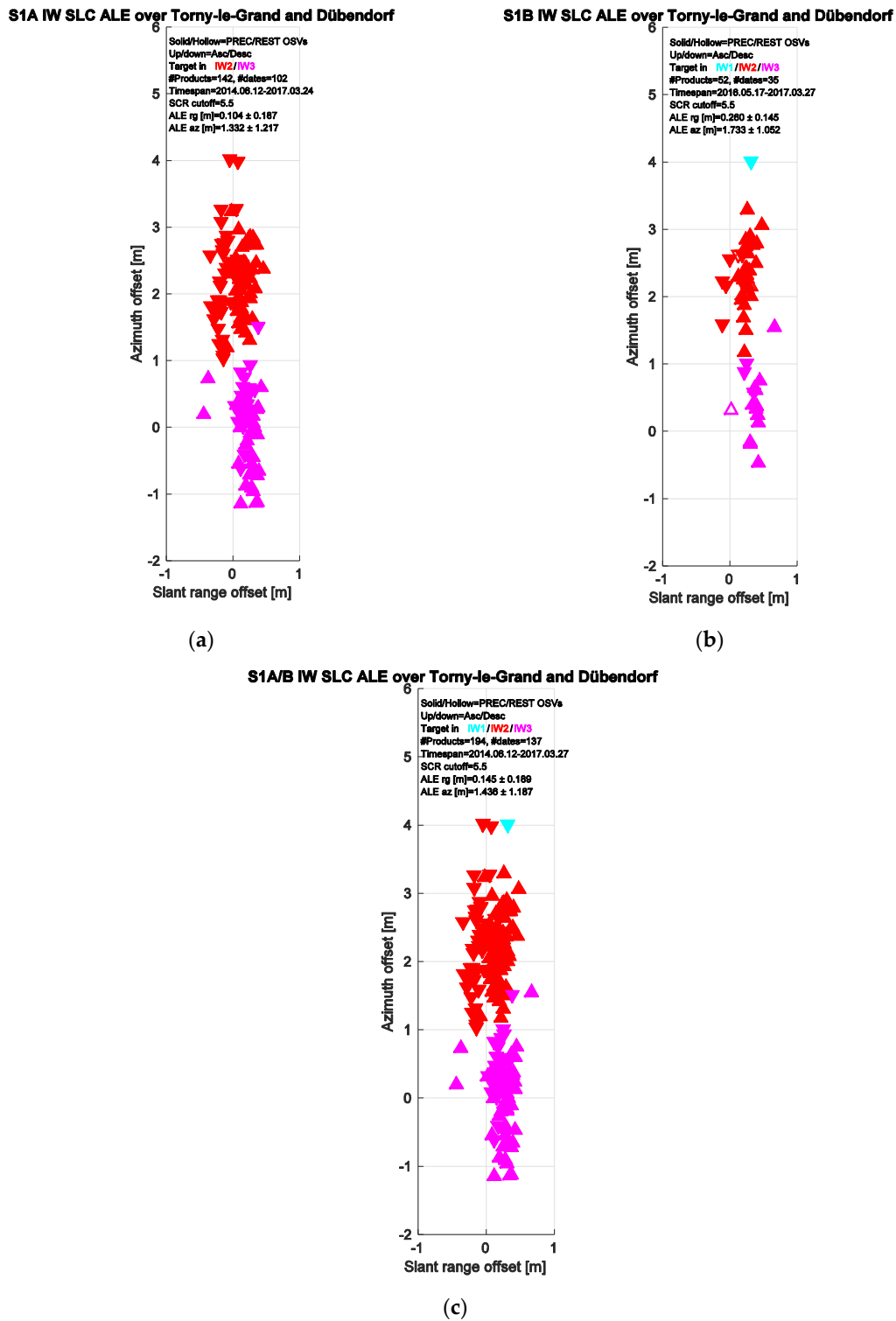


Figure 4. Cont.

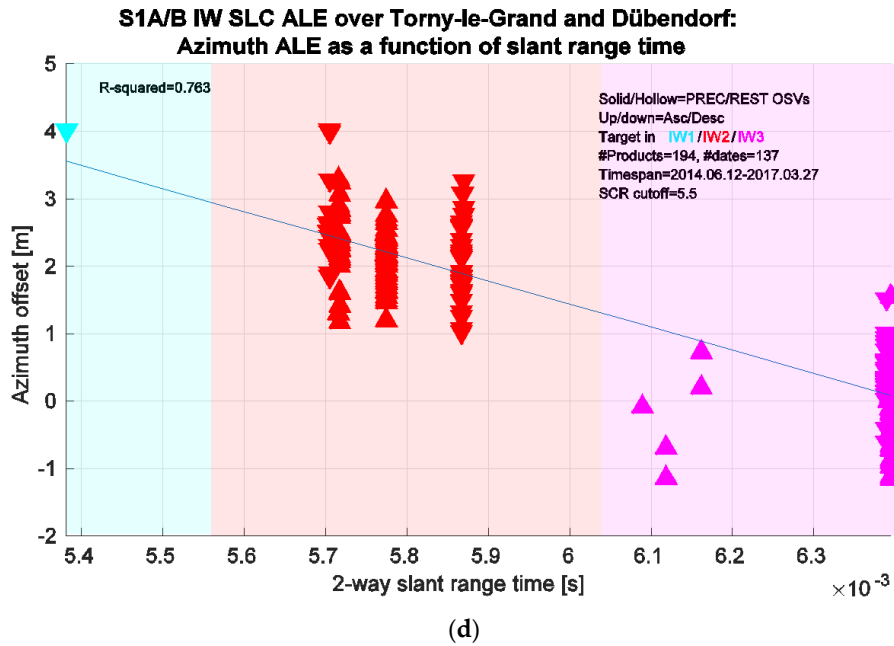


Figure 4. S-1 IW mode SLC geolocation accuracy based on products acquired over Swiss test sites from 2014 to 2017: (a) S-1A; (b) S-1B; (c) S-1A/B combined; (d) azimuth error vs. slant range time for IW mode SLC products, with least-squares fit. Coloured regions indicate approximate subswath ranges.

3.3. Extended Wide Swath (EW) Mode

For the EW mode, only SLC products from the S-1B unit were available over the Swiss test sites. Given the previously noted compatibility between S-1A and S-1B, we expect the S-1B scatterplot to resemble the S-1A scatter (if it were available). The S-1B scatter is shown in Figure 5.

S1B EW SLC ALE over Torny-le-Grand and Dübendorf

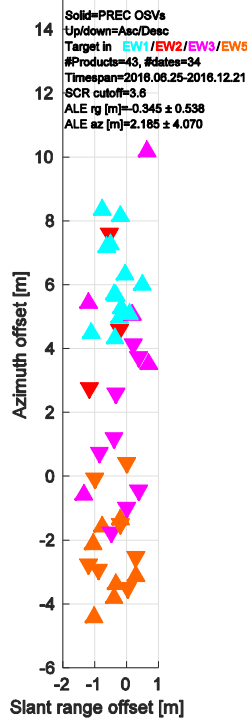


Figure 5. Cont.

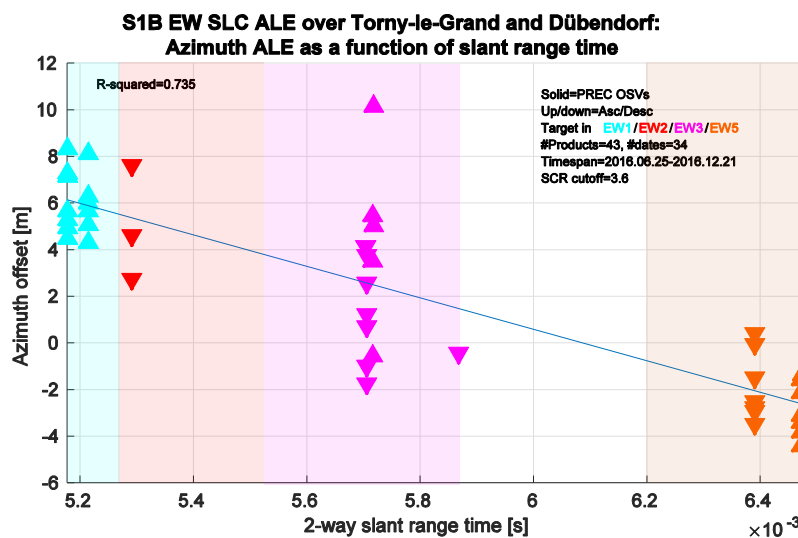


Figure 5. S-1B EW mode SLC geolocation accuracy based on products over Swiss test sites in 2016: (a) S-1B (no S-1A products available); (b) azimuth error vs. slant range time for EW mode SLC products, with least-squares fit. Coloured regions indicate approximate subswath ranges (except EW4).

Again, a subswath-dependent azimuth offset appears to exist, although the slope of the trend is much steeper in comparison with the IW trend from Figure 4d (~ -7.7 m/ms for EW compared with ~ -3.5 m/ms for IW). As with the comparison between the SM and IW modes, the significant difference in the trend lines for the IW and EW modes seems to contradict the idea of a physical correlation between the azimuth offset and the slant range. The hypothesis of a pure beam-dependent offset is therefore given further weight by the EW analysis.

4. Validation Using the Australian Surat Corner Reflector Array

As part of the ongoing cooperation between the ESA and GSA, the suitability of the Surat Basin CR test site for geometric calibration purposes was assessed, and comparisons made with the Swiss sites. Until November 2016, a typical ALE scatterplot for an IW SLC time series spanning several months looked like the one shown in Figure 6. Not only were the absolute offset and standard deviation high in comparison with the IW SLC results obtained over the Swiss test sites, a correlation between the ALE and the dates of the original CR surveys had been shown to exist (symbol colour-coding in Figure 6; the numbers indicate specific CRs). This knowledge led to an internal investigation by GSA, which ended with the discovery of a data download error that had occurred during the original survey. The error was rectified retrospectively, and a new set of corrected reflector coordinates published (see the supplementary papers connected to [19]).

The ALE scatterplot generated using the updated target coordinates is shown in Figure 7, with symbols coloured and labeled according to the site number defined by GSA. When compared with Figure 6, the range and azimuth ALE have improved dramatically. However, the feature most immediately identifiable is the (expected) separation between the points from the targets in either subswath IW1 (upper group) or subswath IW2 (lower group). This effect was discussed previously for the IW time series over the Swiss sites (see also Figure 4c).

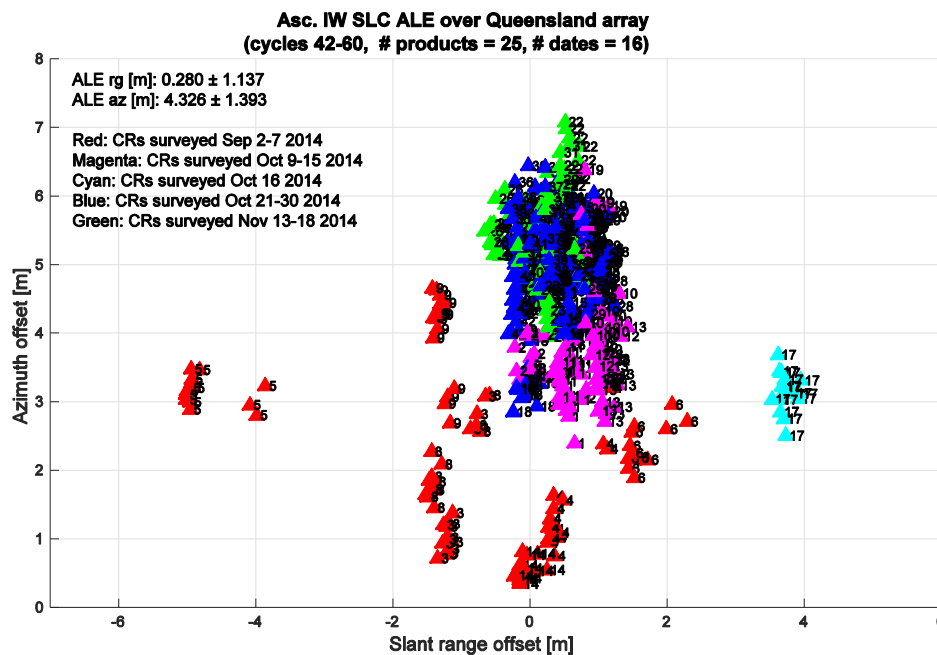


Figure 6. S-1 IW mode SLC product geolocation accuracy based on 25 products acquired over Australian Surat corner reflector (CR) array from March–October 2015, *before* correction of the original GPS survey download errors. Colour-coding indicates survey period; the symbol numbers indicate specific reflector IDs.

The IW SLC product ALE for this time series was measured to be:

Slant range error = -0.04 ± 0.25 m

Total azimuth error = 3.59 ± 0.91 m

- IW1 azimuth error = 4.30 ± 0.36 m
- IW2 azimuth error = 2.58 ± 0.27 m

When compared with the geolocation results obtained from the analysis of the IW SLC data acquired over the Swiss test sites (Figure 4), three significant differences were observed.

First, the lower azimuth standard deviation (0.90 m compared with 1.19 m) is largely explained by the lack of measurements in Australia from subswath IW3, which would otherwise generate a third “cloud” underneath the IW2 cloud in Figure 7.

Second, the mean azimuth offset of the IW2 “cloud” differs noticeably: 2.25 m in Switzerland and 2.58 m in Australia, i.e., a 33 cm difference. IW1 cannot be compared, as only one measurement is available over Switzerland. This difference is not insignificant; it is currently under investigation.

Finally, the range standard deviation of 0.25 m was somewhat higher than the comparable value for the Swiss time series (0.19 m). This is not surprising, and it highlights a major difference between these datasets. While the Swiss data series consists of a large number of observations of the same four targets from several satellite tracks (of both ascending and descending orbits), the Australian series was acquired from a single, ascending orbital track (relative orbit 111). Thus, while a major source of (presumed to be random) error in the Swiss case was the diversity of tracks corresponding to different viewpoints, for the Surat dataset it was likely the 40 independently surveyed targets themselves, each imaged dozens of times (there were 50 acquisition dates). Also, by acquiring the same ground targets from different orbits (but the same viewing angle) over a long period of time, the impact of potential inaccuracies in the orbit data is reduced due to temporal averaging.

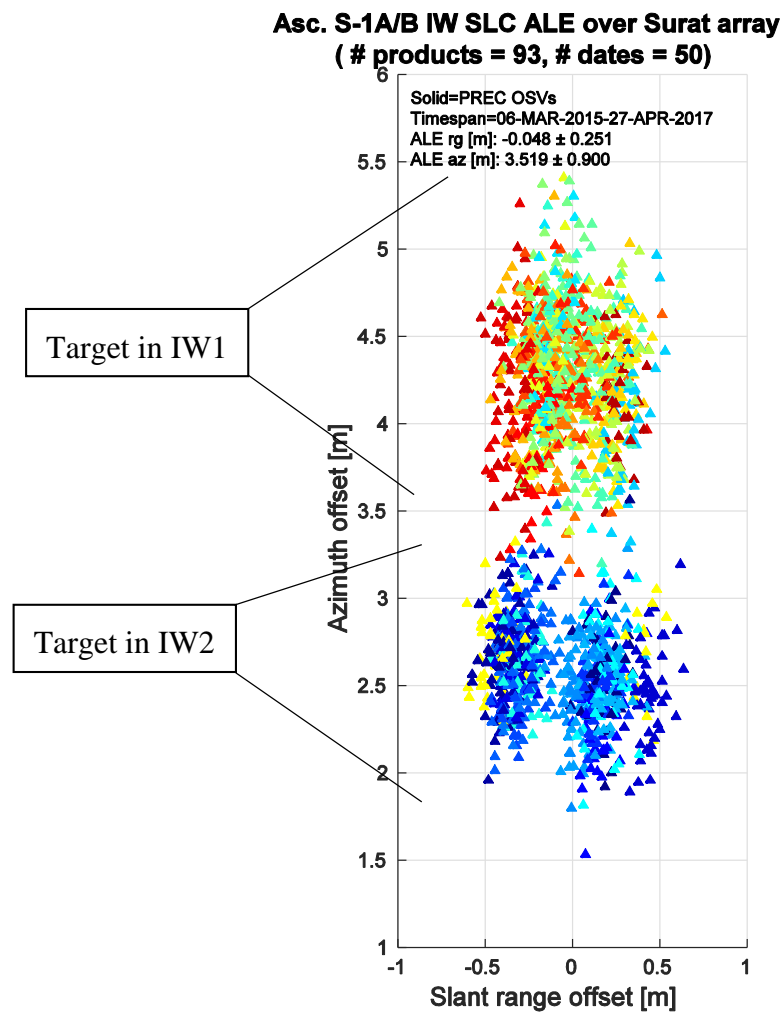


Figure 7. S-1 IW mode SLC product geolocation accuracy based on products over Australian Surat corner reflector array from 2015–2017 after correction of the GPS download error during the original survey. Colours indicate specific reflectors in the array.

A significant feature in the Surat analysis is not directly visible in Figure 7, and it provides convincing support for the hypothesis proposed in the previous sections; namely, that there appears to be a subswath-dependent azimuth offset. This can be demonstrated with the Surat time series by looking at the scatter for individual reflectors at different ranges within the same subswath. It turns out that there is no correlation between azimuth offset and slant range within a subswath: only the scatter clouds for the subswaths themselves are offset relative to each other, and in a manner that appears to be correlated with the slant range (albeit differently for each imaging mode). With this additional observation from the Surat data complementing the time series over the Swiss sites, we have good reason to believe that consistent subswath- (or beam-) dependent offsets—and not strictly range-dependent offsets—do exist for all of the modes.

5. Discussion

Product geolocation estimates were made based on the SM, IW, and EW mode SLC product time series acquired between 2014 and 2017 over Swiss and Australian test sites. The estimates accounted for known perturbing effects (the atmospheric path delay, the solid Earth tide, and the tectonic drift of the local GPS coordinate frame).

As described in Section 2.2, the ALE specification at 3σ for the SM mode is 2.5 m. For the SM SLC (Figure 3c), this condition is easily met in range, but only just barely met in azimuth due to the current lack of azimuth timing calibration support by the S-1 processor (although this will be remedied soon).

For the IW SLC case, the 3σ accuracy specification is 7 m. As can be seen in Figure 4c, this condition is easily met in range, and is met for azimuth as well, in spite of the hypothesised subswath-dependent offsets.

The EW geolocation requirements are not specified; the current analysis (Figure 5c) puts the 3σ perimeter at ~ 14.4 m.

There appears to be a beam- (or subswath-) dependent azimuth offset in the SLC products from all of the tested modes (SM, IW, and EW). Since the GRD products are derived from the SLC data, they may also be assumed to exhibit this dependency. Moreover, while the beam-to-beam offsets appear to be correlated with the slant range for a given mode, the offsets for imaged targets are not strictly slant range-dependent, as demonstrated by: (a) the lack of correlation with range within a given beam/subswath; and (b) the very different slopes measured for the azimuth ALE vs. slant range plots for the three different modes.

No plausible mechanism or cause has yet been discovered that could explain this behavior, especially in light of the differences in how strongly it manifests itself in the different imaging modes. Further study is needed to shed light on the source.

Proposed Azimuth Correction Procedure

In view of the demonstrated beam-dependent azimuth offsets, we propose an azimuth correction approach reflecting this knowledge. Although the operational S-1 processor does not currently provide azimuth-calibrated products, future versions of the S-1 processor are expected to include provisions for the incorporation of an azimuth timing calibration constant(s). We therefore propose that the best available data be collected over suitable test sites (such as the ones over Switzerland and Australia), and beam-specific azimuth timing offsets be incorporated into the operational S-1 processor, pending an investigation into the apparent difference between the Swiss and Australian datasets for the IW2 subswath. The ESA is currently in the process of updating the processor configuration, to introduce a dedicated azimuth time calibration constant into the instrument auxiliary files (AUX_INS) used by the processor (expected \sim mid-2017). This should allow the proposed correction to be implemented in the near future. However, parallel investigations will continue to look for the root cause(s) of the observed beam-dependent offsets. The potential causes may include an erroneous interpretation of the instrument timing, further instrument-related issues (considered less likely), or other software-related problems.

For the time series analyses over the Swiss test sites shown in Figures 3–5, the beam-specific mean azimuth offsets were used to move the associated scatter to zero. The resulting modified ALE scatter plots are shown in Figure 8. As long as at least several measurements were available for a given beam/subswath, the mean for those data points was used as the beam offset estimate. The only exception was subswath IW1. As was seen in Figure 4d, only a single measurement for this subswath was available over Switzerland, so the mean offset was obtained instead, from the Australian Surat time series (4.30 m). The plots in Figure 8 illustrate the effect of this kind of azimuth correction. Compared with the equivalent plots in Figures 3c, 4c and 5a, not only have the azimuth offsets been moved to zero, but the azimuth standard deviations have also been reduced.

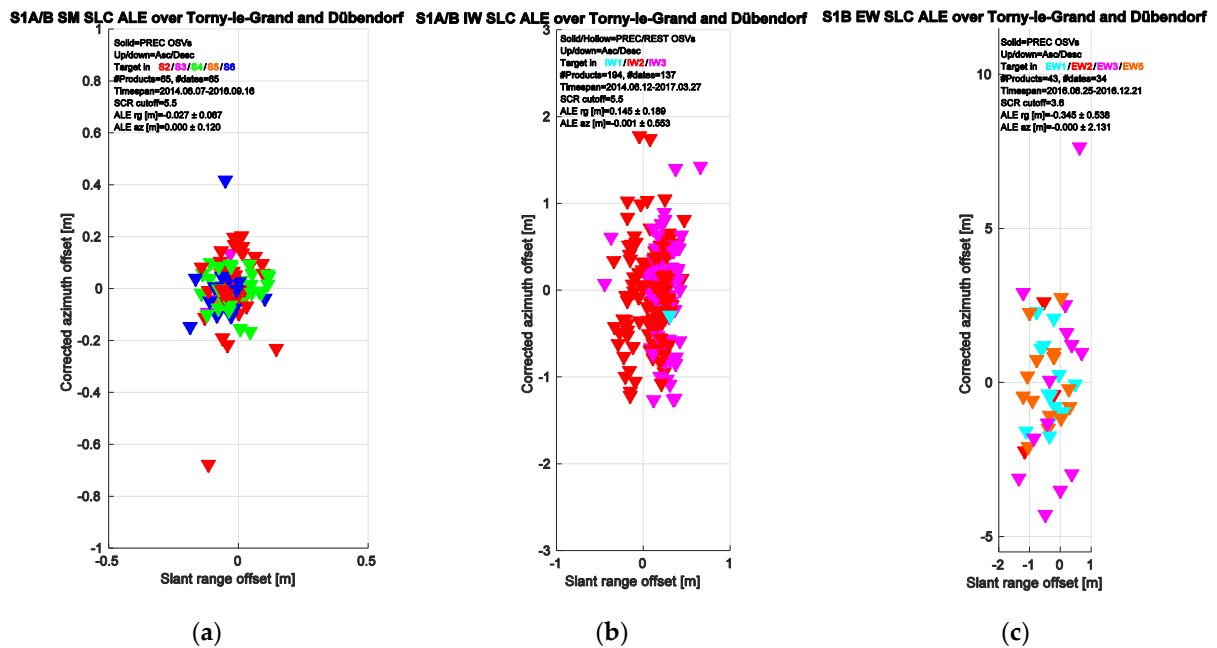


Figure 8. ALE scatterplots of SLC product time series after proposed beam-dependent azimuth correction (a) SM SLC; (b) IW SLC; (c) EW SLC. Compare with uncorrected plots in Figures 3c, 4c and 5a.

An overview of the ALE estimates generated in this study is given in Table 2, along with the azimuth ALE for the SLC products corrected using the measured beam-dependent offsets (where possible). If this type of correction is to be implemented in practice, the best azimuth estimates for each beam/subswath will need to be obtained by the S-1 Mission Performance Centre, based on data acquired over the most suitable test sites. The values obtained in this paper (listed in Table 3) could serve as a starting point, with the exception of the SM beam S1 and the TOPS subswath EW4, for which too little data were available to the authors. It is also hoped that the reason for the observed 33 cm difference between the Swiss and Australian IW SLC measurements (for subswath IW2) will be discovered before the estimation of offsets assumed to be constant. The application of this type of correction would be expected to shift the ALE to well within the product specifications for absolute location error in azimuth.

Table 3. Azimuth offsets (and associated precision) measured for individual beams or subswaths.

| Acq. Mode | Beam/Subswath | Source | Nr. of Contributing Products | Azimuth Offset \pm stdDev [m] |
|-----------|---------------|-------------------------------|------------------------------|---------------------------------|
| SM | S1 | - | - | - |
| | S2 | Swiss S-1A/B time series | 36 | 1.59 \pm 0.16 |
| | S3 | Swiss S-1A time series | 6 | 1.78 \pm 0.08 |
| | S4 | Swiss S-1A/B time series | 32 | 1.96 \pm 0.07 |
| | S5 | Swiss S-1A time series | 4 | 1.81 \pm 0.05 |
| IW | S6 | Swiss S-1A/B time series | 14 | 2.08 \pm 0.14 |
| | IW1 | Australian S-1A/B time series | 99 | 4.30 \pm 0.36 |
| | IW2 | Swiss S-1A/B time series | 122 | 2.25 \pm 0.55 |
| EW | IW3 | Swiss S-1A/B time series | 77 | 0.12 \pm 0.57 |
| | EW1 | Swiss S-1B time series | 13 | 6.05 \pm 1.32 |
| | EW2 | Swiss S-1B time series | 3 | 5.00 \pm 2.45 |
| | EW3 | Swiss S-1B time series | 13 | 2.53 \pm 3.33 |
| | EW4 | - | - | - |
| | EW5 | Swiss S-1B time series | 14 | -2.33 \pm 1.39 |

6. Conclusions and Recommendations

Geolocation accuracy was estimated for S-1A and S-1B SM, IW, and EW product time series acquired over test sites in Switzerland and Australia. When known perturbing effects were taken into account (the atmospheric path delay, the solid Earth tide, and the tectonic drift of the local GPS

coordinate frame), both S-1A and S-1B's SLC products from their SM and IW modes were shown to have accuracies better than the nominal product specifications (the EW accuracy requirements were not originally specified).

The largest remaining artefact found during our analyses appears to be a beam- (or subswath-) dependent azimuth offset. No physical explanation for these offsets has yet been found, although the inter-beam offsets do generally correlate with the slant range dimension. However, the magnitude and direction of the correlation is unique to each mode.

A pragmatic correction (calibration) procedure has been proposed to minimise the observed azimuth biases, with preliminary improvements shown. We recommend that this method is implemented in future releases of the operational S-1 processor, with the most accurate available beam/subswath-specific offsets to be determined by the S-1 Mission Performance Centre.

Acknowledgments: The work described in this paper was in part funded by ESA Contracts 4000110757/14/NL/MP/ab and 4000114792/14/N5/MP/. The activities were also realised as part of the Sentinel-1 Mission Performance Centre project (ESA/CLS reference 4000107360/12/I-LG), funded by the European Union as part of the Copernicus program.

Author Contributions: All authors conceived and designed the experiments; A. Schubert performed the experiments and analyzed the data described in the study with help from D. Small; D. Geudtner contributed parts of the introductory text; D. Geudtner, N. Miranda and D. Small commented on the manuscript and made useful suggestions; A. Schubert wrote the paper.

Conflicts of Interest: The authors declare no conflict of interest.

Abbreviations

The following abbreviations are used in this manuscript:

| | |
|----------|--|
| ALE | Absolute Location Error |
| APD | Atmospheric Path Delay |
| ASAR | Advanced Synthetic Aperture Radar |
| DEM | Digital Elevation Model |
| DLR | <i>Deutsches Zentrum für Luft- und Raumfahrt</i> (German Aerospace Centre) |
| ESA | European Space Agency |
| EW | Extended Wide swath (Sentinel-1 imaging mode) |
| GNSS | Global Navigation Satellite Systems |
| GPS | Global Positioning System |
| GRD(F/H) | Ground Range Detected (Fine/High resolution) |
| GSA | Geoscience Australia |
| InSAR | Interferometric Synthetic Aperture Radar |
| IPF | Instrument Processing Facility |
| IW | Interferometric Wide swath (Sentinel-1 imaging mode) |
| S-1(A/B) | Sentinel-1(A/B) |
| SAR | Synthetic Aperture Radar |
| SCR | Signal-to-Clutter Ratio |
| SET | Solid Earth Tide |
| SLC | Single Look Complex |
| SM | StripMap (Sentinel-1 imaging mode) |
| TOPS | Terrain Observation by Progressive Scans |
| TSX | TerraSAR-X |

References

1. Torres, R.; Snoeij, P.; Geudtner, D.; Bibby, D.; Davidson, M.; Attema, E.; Potin, P.; Rommen, B.; Floury, N.; Brown, M.; et al. GMES Sentinel-1 mission. *Remote Sens. Environ.* **2012**, *120*, 9–24. [[CrossRef](#)]
2. Geudtner, D.; Torres, R.; Snoeij, P.; Davidson, M. Sentinel-1 System Overview. In Proceedings of the 9th European Conference on Synthetic Aperture Radar, Nürnberg, Germany, 23–26 April 2012; pp. 159–161.

3. Schubert, A.; Small, D.; Jehle, M.; Meier, E. COSMO-SkyMed, TerraSAR-X, and Radarsat-2 Geolocation Accuracy after Compensation for Earth-System Effects. In Proceedings of the 2012 IEEE International Geoscience and Remote Sensing Symposium (IGARSS 2012), Munich, Germany, 22–27 July 2012; pp. 3301–3304.
4. Barnhart, W.D.; Lohman, R.B. Characterizing and estimating noise in InSAR and InSAR time series with MODIS. *Geochem. Geophys. Geosyst.* **2013**, *14*, 4121–4132. [[CrossRef](#)]
5. Small, D.; Rosich, B.; Schubert, A.; Meier, E.; Nüesch, D. Geometric Validation of Low and High-Resolution ASAR Imagery. In Proceedings of the ESA ENVISAT and ERS Symposium, Salzburg, Austria, 6–10 September 2004; pp. 1–9.
6. Small, D.; Rosich, B.; Meier, E.; Nüesch, D. Geometric Calibration and Validation of ASAR Imagery. In Proceedings of the CEOS WGCV SAR Calibration & Validation Workshop, Ulm, Germany, 27–28 May 2004; pp. 1–8.
7. Schubert, A.; Small, D.; Miranda, N.; Geudtner, D.; Meier, E. Sentinel-1A Product Geolocation Accuracy: Beyond the Calibration Phase. In Proceedings of the CEOS SAR Calibration & Validation Workshop, Noordwijk, The Netherlands, 27–29 October 2015; Volume 7, pp. 9431–9449.
8. Schwerdt, M.; Schmidt, K.; Ramon, N.T.; Alfonzo, G.C.; Döring, B.; Zink, M.; Prats, P. Independent verification of the Sentinel-1A system calibration. *IEEE J. Sel. Top. Appl. Earth Obs. Remote Sens.* **2016**, *9*, 994–1007. [[CrossRef](#)]
9. Schubert, A.; Small, D.; Miranda, N.; Geudtner, D.; Meier, E. Sentinel-1A Product Geolocation Accuracy: Commissioning Phase Results. *Remote Sens.* **2015**, *7*, 9431–9449. [[CrossRef](#)]
10. Mancon, S.; Monti Guarnieri, A.; Giudici, D.; Tebaldini, S. On the Phase Calibration by Multisquint Analysis in TOPSAR and Stripmap Interferometry. *IEEE Trans. Geosci. Remote Sens.* **2017**, *55*, 134–147. [[CrossRef](#)]
11. Schubert, A.; Jehle, M.; Small, D.; Meier, E. Geometric Validation of TerraSAR-X High-Resolution Products. In Proceedings of the 3rd TerraSAR-X Science Team Meeting, Oberpfaffenhofen, Germany, 25–26 November 2008.
12. Schubert, A.; Jehle, M.; Small, D.; Meier, E. Influence of Atmospheric Path Delay on the Absolute Geolocation Accuracy of TerraSAR-X High-Resolution Products. *IEEE Trans. Geosci. Remote Sens.* **2010**, *48*, 751–758. [[CrossRef](#)]
13. Schubert, A.; Jehle, M.; Small, D.; Meier, E. Mitigation of atmospheric perturbations and solid Earth movements in a TerraSAR-X time-series. *J. Geod.* **2012**, *86*, 257–270. [[CrossRef](#)]
14. Reinartz, P.; Müller, R.; Suri, S.; Schwind, P. Improving geometric accuracy of optical VHR satellite data using terrasarsar-X data. *IEEE Aerosp. Conf. Proc.* **2010**. [[CrossRef](#)]
15. Gisinger, C.; Willberg, M.; Balss, U.; Klügel, T.; Mähler, S.; Pail, R.; Eineder, M. Differential geodetic stereo SAR with TerraSAR-X by exploiting small multi-directional radar reflectors. *J. Geod.* **2016**, *91*, 53–67. [[CrossRef](#)]
16. Small, D. Flattening Gamma: Radiometric Terrain Correction for SAR Imagery. *IEEE Trans. Geosci. Remote Sens.* **2011**, *49*, 3081–3093. [[CrossRef](#)]
17. Small, D.; Biegger, S.; Nüesch, D. Automated Tiepoint Retrieval Through Heteromorphic Image Simulation for Spaceborne SAR Sensors. In Proceedings of the ESA ERS-ENVISAT Symposium, Gothenburg, Sweden, 16–20 October 2000; p. 8.
18. Miranda, N.; Meadows, P.J.; Pilgrim, A.; Piantanida, R.; Recchia, A.; Giudici, D.; Small, D.; Schubert, A. Sentinel-1B Preliminary Results Obtained During the Orbit Acquisition Phase [Work in Progress]. *Procedia Comput. Sci.* **2016**, *100*, 1313–1318. [[CrossRef](#)]
19. Garthwaite, M.C.; Hazelwood, M.; Nancarrow, S.; Hislop, A.; Dawson, J.H. A regional geodetic network to monitor ground surface response to resource extraction in the northern Surat Basin, Queensland. *Aust. J. Earth Sci.* **2015**, *62*, 469–477. [[CrossRef](#)]
20. Bourbigot, M.; Johnson, H.; Piantanida, R. *Sentinel-1 Product Definition*; MDA Document Number: SEN-RS-52-7440; ESA CDRL Number: PDL1-1, PDL2-1; MacDonald, Dettwiler and Associates Ltd.: Richmond, BC, Canada, 2016.

